Soluble two-dimensional photonic-crystal model

T. J. Shepherd and P. J. Roberts
Defence Research Agency, Malvern, Worcs WR14 3PS, England

Rodney Loudon
Physics Department, University of Essex, Colchester CO4 3SQ, England
(Received 20 September 1996)

We present an analytical treatment of a two-dimensional square photonic lattice constructed from two infinite arrays of dielectric sheets at right angles, in the limit of very small sheet thickness and very high dielectric constant, such that their product is constant. The photonic band structures for s- and p-polarized electromagnetic waves are calculated analytically. This approach enables two varieties of band to be identified and understood in terms of locally propagating and locally evanescent field distributions in the primitive cell. The densities of states are interpreted in terms of one- and two-dimensional contributions from the two kinds of band. As preliminaries to the two-dimensional calculations, we derive the photonic properties of the single dielectric sheet and of the infinite one-dimensional array of such sheets. [S1063-651X(97)07904-X]

PACS number(s): 42.70.Qs, 41.20.Jb, 77.90.+k

I. INTRODUCTION

The considerable current interest in the band structures that govern the propagation of electromagnetic waves through ordered dielectric crystals [1–4] stems from potentially useful applications in the improvement of semiconductor laser sources. The existence of a forbidden gap at the laser transition frequency can remove unwanted spontaneous emission and greatly improve the efficiency of the device. The first demonstration by Yablonovitch and co-workers [5] of a photonic band gap at microwave frequencies has stimulated many theoretical efforts to understand the behavior of the electromagnetic field in composite dielectrics and to identify crystal structures with significant band gaps. On the experimental side, the challenge is to fabricate these structures on a sufficiently small scale to affect the photon emission characteristics at the infrared or visible frequencies important in practical lasers.

Calculations of photonic band structures in one dimension can be performed analytically [6], but treatments in two or more dimensions have almost all used numerical techniques to integrate Maxwell's equations. Amongst the numerical methods, k-space expansion techniques were first used by Leung and Liu [7], Zhang and Satpathy [8], and Ho, Chan, and Soukoulis [9], the more versatile transfer matrix approach has been developed by Pendry and MacKinnon [10,11], and Stefanou, Karathanos, and Modinos [12] have applied an electromagnetic version of the Korringa-Kohn-Rostoker method. These various numerical calculations have produced a wealth of information on the photonic bands associated with a range of composite dielectric structures.

In contrast to earlier work, our aim in this paper is to present analytic calculations of the propagation of electromagnetic waves through a simple form of two-dimensional dielectric crystal. The structure takes the form of a square lattice of very thin, high dielectric constant sheets, similar to the two-dimensional version [13] of the Kronig-Penney model [14] familiar in the treatment of electronic energy bands in crystals. This form of crystal has previously been treated numerically by Meade and co-workers [3,15] and brief details of our own calculations have been reported [16]. The main advantages of an analytic approach are the physical insight into the nature and significance of the photonic bands and the ease of computation of the band structure and density of states. Although the dielectric crystal considered here is a limiting form of what could be fabricated in practice, its structure can be approached by practical samples and its photonic properties resemble those of more realistic dielectric crystals.

The calculations are heavily dependent on the optical properties of the single dielectric sheets from which the two-dimensional structure is formed, particularly the waveguide modes, and these are treated in Sec. II. The one-dimensional lattice, or Bragg stack, of these sheets is briefly considered in Sec. III, and it is shown that there are two kinds of propagating Bloch waves, constructed, respectively, from fields that have locally propagating and locally evanescent characters in the individual primitive cells of the lattice. The main calculations on the two-dimensional lattice are presented in Sec. IV, where it is shown that the same two kinds of Bloch waves occur. Many features of the photonic band dispersion relations and their densities of states are calculated analytically. The conclusions of the work are summarized in Sec. V.

II. DIELECTRIC SHEET

The one-dimensional lattice treated in Sec. III and the two-dimensional lattice treated in Sec. IV are formed from dielectric sheets of thickness d and relative permittivity ε, taken in the limits

$$d \to 0, \quad \varepsilon \to \infty \quad \text{such that} \quad \varepsilon d \equiv m = \text{const.} \tag{2.1}$$

The quantity m defined in this way has the dimensions of length, and it provides a single-parameter characterization of the dielectric sheets in the limit of infinitesimal thickness. In the present section, we consider the boundary conditions and

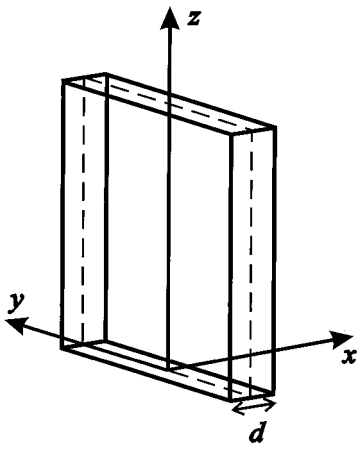

FIG. 1. Geometrical arrangement of a single slab showing the coordinate axes.

the waveguide modes for a single sheet in this limiting case. Such sheets have been used before to model the mirrors of Fabry-Pérot cavities [17], but we need here to extend previous work to cover oblique incidence and waveguide modes.

A. Boundary conditions

Figure 1 shows the arrangement of a dielectric slab, which is assumed initially to have a nonzero thickness d and a finite relative permittivity ε, and the orientations of the coordinate axes. The slab is assumed to have vacuum on either side, and the fields just outside the slab at $x<0$ and $x>0$ are indicated by superscripts $<$ and $>$, respectively. The boundary conditions for the slab as a whole can be determined by the application of the usual boundary conditions to its separate surfaces. Alternatively, the boundary conditions can be found in a single calculation with the help of an imaginary cylinder whose axis lies at right angles to the slab and whose ends just protrude through its surfaces. It is found after imposition of the limit given in Eq. (2.1) that the tangential components of the electric field are continuous,

$$E_y^{>}=E_y^{<}, \quad E_z^{>}=E_z^{<}, \tag{2.2}$$

but the normal component suffers a discontinuity,

$$E_x^{>}=E_x^{<}-m\left(\frac{\partial E_y}{\partial y}+\frac{\partial E_z}{\partial z}\right), \tag{2.3}$$

where no superscripts are needed on the y and z component fields in view of Eq. (2.2). For the magnetic field, the normal component is continuous,

$$H_x^{>}=H_x^{<}, \tag{2.4}$$

but the tangential components suffer discontinuities,

$$H_y^{>}=H_y^{<}+\varepsilon_0 m\,\frac{\partial E_z}{\partial t}, \quad H_z^{>}=H_z^{<}-\varepsilon_0 m\,\frac{\partial E_y}{\partial t}. \tag{2.5}$$

The field discontinuities expressed by Eqs. (2.3) and (2.5) can be written more generally in the coordinate-independent forms

$$\Delta\mathbf{E}=-m\mathbf{n}(\mathbf{n}\times\boldsymbol{\nabla})\cdot(\mathbf{n}\times\mathbf{E}) \tag{2.6}$$

and

$$\Delta\mathbf{H}=-\varepsilon_0 m\mathbf{n}\times\frac{\partial\mathbf{E}}{\partial t}, \tag{2.7}$$

where $\Delta\mathbf{E}$ and $\Delta\mathbf{H}$ are the increments in the fields in passing through the dielectric sheet in the direction of the unit vector $\mathbf{n}$ normal to its surfaces. It should be noted that in applications of Eqs. (2.6) and (2.7), some components of one boundary condition may duplicate some of the other. Since all of the Maxwell equations (including both divergence equations) are used in the derivation of Eqs. (2.6) and (2.7), this simply reflects the redundancy present in Maxwell's equations in the absence of sources.

The boundary conditions derived above can be used to determine the reflection and transmission coefficients for monochromatic light of frequency ω incident on the sheet. For s polarization the electric vectors of the incident, reflected and transmitted fields are parallel to the sheet surfaces, and the coefficients that relate the outgoing electric and magnetic field amplitudes to the incident amplitudes are

$$r_s=\frac{imk^2/2k_x}{1-i(mk^2/2k_x)}, \quad t_s=\frac{1}{1-i(mk^2/2k_x)}. \tag{2.8}$$

For p polarization the magnetic vectors of the incident, reflected and transmitted fields are parallel to the sheet surfaces, and the coefficients that relate the outgoing electric- and magnetic-field amplitudes to the incident amplitudes are

$$r_p=\frac{-imk_x/2}{1-i(mk_x/2)}, \quad t_p=\frac{1}{1-i(mk_x/2)}. \tag{2.9}$$

In these expressions, $k=\omega/c$ is the magnitude of the vacuum wave vector and k_x is its component normal to the dielectric sheet. The sheet is isotropic in the yz plane, and we arbitrarily take k_y to be the component of the vacuum wave vector parallel to the sheet, with $k_z=0$, so that

$$k_x^2+k_y^2=k^2=\omega^2/c^2. \tag{2.10}$$

The magnitudes of the reflection and transmission coefficients cover the complete range of values between 0 and 1 as the parameter m is varied between 0 and ∞. It is easily verified that both sets of coefficients satisfy the requirements

$$|r|^2+|t|^2=1, \quad r^*t+rt^*=0 \tag{2.11}$$

for a unitary transformation between input and output amplitudes at the sheet.

B. Waveguide modes

We are interested in the waves that propagate along the dielectric sheet under conditions of total internal reflection. For a finite-thickness dielectric slab, these waveguide modes are considered for example by Yeh [6], but we need to determine which modes survive in the limit given in Eq. (2.1). We again assume initially that the dielectric slab has a thick-

ness d and a finite relative permittivity ε. It is necessary to consider the two independent transverse polarizations separately.

For s polarization the electric fields in the three spatial regions are taken in the forms

$$\mathbf{E}(\mathbf{r},t)=\hat{\mathbf{z}}E(x)e^{ik_y y-i\omega t}, \tag{2.12}$$

with traveling-wave behavior inside the dielectric and evanescent decay on either side,

$$E(x)=\begin{cases} Ae^{q_x(x+d/2)} & x<-\frac{1}{2}d \\ Be^{i\kappa x}+Ce^{-i\kappa x} & -\frac{1}{2}d<x<\frac{1}{2}d \\ De^{-q_x(x-d/2)} & \frac{1}{2}d<x, \end{cases} \tag{2.13}$$

where k_x has been replaced by iq_x, and q_x must be positive for a properly guided excitation of the electromagnetic field. We have again taken $k_z=0$, and the relation (2.10) between the wave-vector components in vacuum is now modified to

$$-q_x^2+k_y^2=\omega^2/c^2, \tag{2.14}$$

while the components in the dielectric slab satisfy

$$\kappa^2+k_y^2=\varepsilon\omega^2/c^2. \tag{2.15}$$

The waveguide modes are characterized by the property that their wave-vector component k_y, parallel to the surfaces of the slab, is larger than the total free-space wave vector ω/c. Elimination of the common wave-vector component k_y from Eqs. (2.14) and (2.15) gives

$$\kappa^2+q_x^2=(\varepsilon-1)\omega^2/c^2. \tag{2.16}$$

The constants A, B, C, and D in Eq. (2.13) are related by the usual boundary conditions at the two surfaces of the slab, and the consistency condition for the four resulting relations takes the form

$$e^{2i\kappa d}=\left(\frac{\kappa+iq_x}{\kappa-iq_x}\right)^2, \tag{2.17}$$

with the solutions

$$\tan(\kappa d/2)=q_x/\kappa \tag{2.18}$$

corresponding to symmetric mode functions and the solutions

$$\tan(\kappa d/2)=-\kappa/q_x \tag{2.19}$$

corresponding to the antisymmetric mode functions. These two trigonometric relations in conjunction with Eq. (2.16) determine the wave vectors for the guided modes of the dielectric slab with s polarization.

Consider now the sheet of infinitesimal thickness defined by the limit given in Eq. (2.1). It is helpful to parametrize κ and q_x in Eq. (2.16) by

$$\kappa=(\varepsilon-1)^{1/2}(\omega/c)\cos\vartheta,$$

$$q_x=(\varepsilon-1)^{1/2}(\omega/c)\sin\vartheta, \tag{2.20}$$

so that Eq. (2.18) takes the form

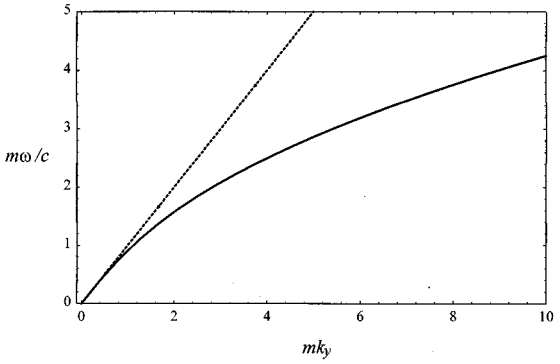

FIG. 2. Single-sheet dispersion relation ω vs the wave-vector component k_y parallel to the surfaces, for the guided modes in infinitesimal sheets. The broken line shows the free-space dispersion relation.

$$\tan[(\varepsilon-1)^{1/2}(m\omega/2\varepsilon c)\cos\vartheta]=\tan\vartheta, \tag{2.21}$$

and when $\varepsilon\to\infty$ the angle ϑ tends to zero according to

$$\vartheta=m\omega/2\varepsilon^{1/2}c. \tag{2.22}$$

This is the only solution of the equations for the symmetric mode functions that survives in the limit. It follows from Eq. (2.20) that the internal propagating wave vector κ tends to infinity according to

$$\kappa=\varepsilon^{1/2}\omega/c, \tag{2.23}$$

and the vacuum evanescent wave vector q_x takes the limiting form

$$q_x\to m\omega^2/2c^2\equiv q. \tag{2.24}$$

Elimination of q_x from Eq. (2.14) now produces the relation between the mode frequency ω and the propagating wave-vector component k_y parallel to the surfaces in the form

$$\frac{\omega}{c}=\left(\frac{(1+m^2k_y^2)^{1/2}-1}{m^2/2}\right)^{1/2}. \tag{2.25}$$

This is the single-sheet dispersion relation and Fig. 2 shows the variation of ω with k_y together with the free-space dispersion relation. A similar procedure can be followed for the antisymmetric modes determined by Eq. (2.19), when $\tan\vartheta$ in Eq. (2.21) is replaced by $-\cot\vartheta$, but the resulting condition has no solutions in the limit $\varepsilon\to\infty$.

For p polarization the magnetic fields are taken in the form

$$\mathbf{H}(\mathbf{r},t)=\hat{\mathbf{z}}H(x)e^{ik_y y-i\omega t}, \tag{2.26}$$

where the expressions for the magnetic fields in the three spatial regions are similar to those for the electric fields given in Eq. (2.13). An analysis of the boundary conditions similar to that used for s polarization leads to the relations

$$\tan(\kappa d/2)=\varepsilon q_x/\kappa \tag{2.27}$$

and

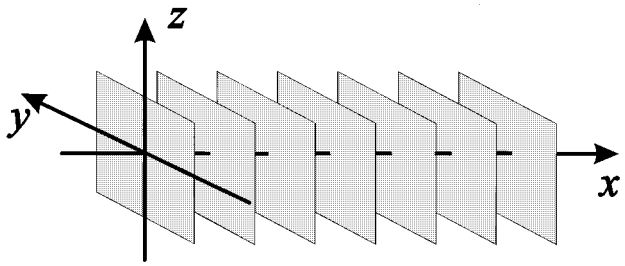

FIG. 3. Geometrical arrangement of the one-dimensional array of infinitesimal sheets.

$$\tan(\kappa d/2) = -\kappa/\varepsilon q_x \tag{2.28}$$

analogous to Eqs. (2.18) and (2.19). The only surviving mode in the limit $\varepsilon \to \infty$ now comes from the antisymmetric condition (2.28); the propagating wave vector inside the dielectric slab is again given by Eq. (2.23) but the evanescent vacuum wave vector now takes the limiting form

$$q_x \to -2/m. \tag{2.29}$$

This negative value ordinarily produces an unacceptable field distribution whose amplitude increases with distance from the dielectric sheet, although the mode would take on a guided nature in the case of a material with negative ε, when the s-polarization guided mode derived above acquires an unacceptable spatial dependence. Negative values of ε occur for frequencies below the plasma frequency in metallic sheets and more generally for frequencies just above the transverse resonances in the dielectric functions of a range of materials [18].

In summary, the dielectric sheet of infinitesimal thickness supports a single guided wave with s polarization, whose frequency and wave-vector components are related by Eqs. (2.14), (2.24), and (2.25). There is no guided wave with p polarization.

III. ONE-DIMENSIONAL LATTICE

We consider in this section the photonic band structure in an infinite one-dimensional array of the infinitesimal dielectric sheets described in Sec. II. The array of sheets with period a is specified by the dielectric function

$$\varepsilon(\mathbf{r}) = 1 + m \sum_{n=-\infty}^{\infty} \delta(x - na), \tag{3.1}$$

and its spatial arrangement is shown in Fig. 3. One-dimensional structures have previously been extensively treated by many authors, including Yeh [6], Born and Wolf [18], and Russell, Birks, and Lloyd-Lucas [19], while Dowling and Bowden [20] have given some results for the limit of infinitesimal sheets. The discussion here is confined to a presentation of material that is needed for the two-dimensional lattice theory of Sec. IV, and some relevant aspects not covered by the earlier work, particularly for the limit given in Eq. (2.1).

A. Locally propagating modes

Consider first s polarization, where the electric field in the region of the primitive cell defined by the free space between the sheets labeled $n-1$ and n is written in the form

$$\mathbf{E}(\mathbf{r}) = \hat{\mathbf{z}} E_n(\mathbf{r}) = \hat{\mathbf{z}} e^{ik_y y}\{E_n^+ e^{ik_x x} + E_n^- e^{-ik_x x}\} \quad \text{for } (n-1)a < x < na \tag{3.2}$$

and the time dependence $\exp(-i\omega t)$ is understood in all fields. The electric field in the primitive cell is here assumed to have a propagating nature, with a real value for the wave-vector component k_x. The lattice is isotropic in the yz plane, and we have again taken $k_z = 0$. The vacuum wave-vector components k_x and k_y perpendicular and parallel to the sheets are again related by Eq. (2.10). The relations between the fields in adjacent primitive cells can be obtained by application of the boundary conditions at the dielectric sheets, given in Eqs. (2.2) to (2.5), where the magnetic field corresponding to Eq. (3.2) is obtained with the use of the $\nabla \times \mathbf{E}$ Maxwell equation. The resulting relation between the electric-field amplitudes in cells n and $n+1$ is conveniently written in matrix notation as

$$\begin{bmatrix} E_{n+1}^+ \\ E_{n+1}^- \end{bmatrix} = \begin{bmatrix} e^{-ink_x a} & 0 \\ 0 & e^{ink_x a} \end{bmatrix} \times \begin{bmatrix} 1 + i(mk^2/2k_x) & i(mk^2/2k_x) \\ -i(mk^2/2k_x) & 1 - i(mk^2/2k_x) \end{bmatrix} \times \begin{bmatrix} e^{ink_x a} & 0 \\ 0 & e^{-ink_x a} \end{bmatrix} \begin{bmatrix} E_n^+ \\ E_n^- \end{bmatrix}, \tag{3.3}$$

where $k = \omega/c$, as in Eq. (2.10). The product of the second and third matrices on the right is the transfer matrix of the system [11], and its elements are combinations of phase factors and terms that occur in the reflection and transmission coefficients (2.8).

The relation between the electric-field amplitudes given in Eq. (3.3) is entirely derived from the properties of the electromagnetic field and the dielectric sheets, but these same field amplitudes are independently related by Bloch's theorem, which applies generally to all forms of excitation in a periodic structure. For the present system, Bloch's theorem takes the form

$$E_{n+1}(\mathbf{r} + \hat{\mathbf{x}} a) = e^{i\mu_x a} E_n(\mathbf{r}), \tag{3.4}$$

where μ_x is the one-dimensional Bloch wave vector and the primitive-cell electric-field amplitudes are defined in Eq. (3.2). We consider here only propagating Bloch waves where μ_x is real. The Bloch wave vector determines the spatial development of the phase of the photonic excitation as it propagates through the lattice. By contrast, the wave-vector component k_x determines the form of the electromagnetic fields in the individual primitive cell, and we refer to it as the *local* wave vector.

The amplitudes in primitive cell $n+1$ are easily eliminated from Eqs. (3.3) and (3.4), and the resulting pair of equations for the amplitudes in primitive cell n are written in matrix form as

$$\begin{bmatrix} [1+i(mk^2/2k_x)]e^{ik_xa}-e^{i\mu_xa} & i(mk^2/2k_x)e^{-(2n-1)ik_xa} \\ -i(mk^2/2k_x)e^{i(2n-1)k_xa} & [1-i(mk^2/2k_x)]e^{-ik_xa}-e^{i\mu_xa} \end{bmatrix} \begin{bmatrix} E_n^+ \\ E_n^- \end{bmatrix} = 0. \quad (3.5)$$

The determinant of the 2×2 matrix essentially identifies the Bloch exponent $\exp(i\mu_x a)$ as the eigenvalue of the transfer matrix, and the multiplied-out determinant can be written in the form

$$e^{2i\mu_xa}-e^{i\mu_xa}\{[1+i(mk^2/2k_x)]e^{ik_xa} + [1-i(mk^2/2k_x)]e^{-ik_xa}\}+1=0 \quad (3.6)$$

or

$$\cos(\mu_x a)=\cos(k_x a)-(mk^2/2k_x)\sin(k_x a). \quad (3.7)$$

This expression, in conjunction with Eq. (2.10), determines the dispersion relation for the locally propagating modes, that is, the dependence of the frequency ω on the Bloch wave vector μ_x for given values of the transverse wave-vector component k_y, for the propagation of electromagnetic waves through the one-dimensional array of dielectric sheets. The first Brillouin zone of the lattice covers the wave-vector range

$$-\pi/a<\mu_x\leqslant\pi/a, \quad (3.8)$$

and we adopt the usual symbols,

$$\Gamma \quad \text{at } \mu_x=0, \quad X \quad \text{at } \mu_x=\pi/a, \quad (3.9)$$

for the symmetry points in the one-dimensional Brillouin zone. The continuous lines in Fig. 4 show some constant-frequency contours in the μ_x versus k_y plane obtained by solution of Eq. (3.7) with the use of Eq. (2.10), where the Bloch wave vector covers the complete Brillouin zone. This figure is further discussed in Sec. III B.

The dispersion relations simplify considerably at the symmetry points Γ and X, where the maxima and minima of the photonic bands generally occur. Thus for s polarization at the Γ point, Eq. (3.7) provides one set of solutions with the implicit form

$$\tan(k_x a/2)=-mk^2/2k_x \quad (3.10)$$

and one with the explicit form

$$\sin(k_x a/2)=0 \text{ or } k_x a=n\pi \text{ or } \omega=c\sqrt{(n\pi/a)^2+k_y^2}, \quad n=2,4,6,\ldots . \quad (3.11)$$

The corresponding solutions at the X point are

$$\cot(k_x a/2)=mk^2/2k_x \quad (3.12)$$

and

$$\cos(k_x a/2)=0 \text{ or } k_x a=n\pi \text{ or } \omega=c\sqrt{(n\pi/a)^2+k_y^2}, \quad n=1,3,5,\ldots . \quad (3.13)$$

Figure 5(a) shows these solutions in the forms of plots of ω against k_y. Each band is bordered by a curve that corresponds to one of the Γ point solutions from Eq. (3.10) or (3.11) or one of the X point solutions from Eq. (3.12) or (3.13), and these four kinds of solutions occur in rotation as one moves up the frequency axis.

Similar derivations can be made for p polarization, where it is now the magnetic field that has a form analogous to that given in Eq. (3.2) for each primitive cell of the array, and the $\nabla\times\mathbf{H}$ Maxwell equation is used to obtain the corresponding electric fields. The boundary conditions (2.2)–(2.5) are again used to relate the fields in adjacent cells, and Bloch's theorem (3.4) again provides an independent connection between these fields. The resulting dispersion relation for p polarization is

$$\cos(\mu_x a)=\cos(k_x a)-\tfrac{1}{2}mk_x\sin(k_x a), \quad (3.14)$$

and this is used in conjunction with Eq. (2.10) to obtain the variation of ω with k_y. Simple results for the Γ and X dispersion relations are found from Eq. (3.14) and indeed two of the expressions are identical to the explicit forms (3.11) and (3.13) obtained for s polarization. The value $n=0$ is additionally allowed in Eq. (3.11) for p polarization and this gives the so-called light line $\omega=ck_y$. The other two expressions are similar to the implicit forms (3.10) and (3.12) but with the quantity $mk^2/2k_x$ replaced by $mk_x/2$. Figure 5(b) shows the band edge diagram for p polarization. The lower boundaries of all except the lowest band are the same for s and p polarizations.

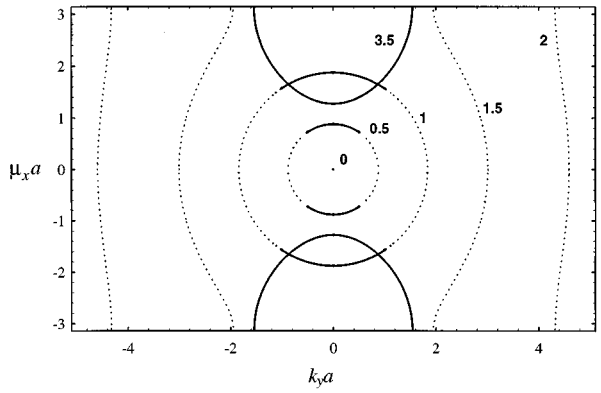

FIG. 4. Constant-frequency contours in the μ_x vs k_y plane for modes with s polarization in a one-dimensional array of infinitesimal sheets. The continuous lines show locally propagating solutions and the broken lines show locally evanescent solutions. The numbers attached to the curves show the values of $\omega a/c$.

B. Locally evanescent modes

The modes discussed above have locally propagating characters in the individual primitive cells, as the local wave vector k_x is assumed to be real. The theory presented in Sec.

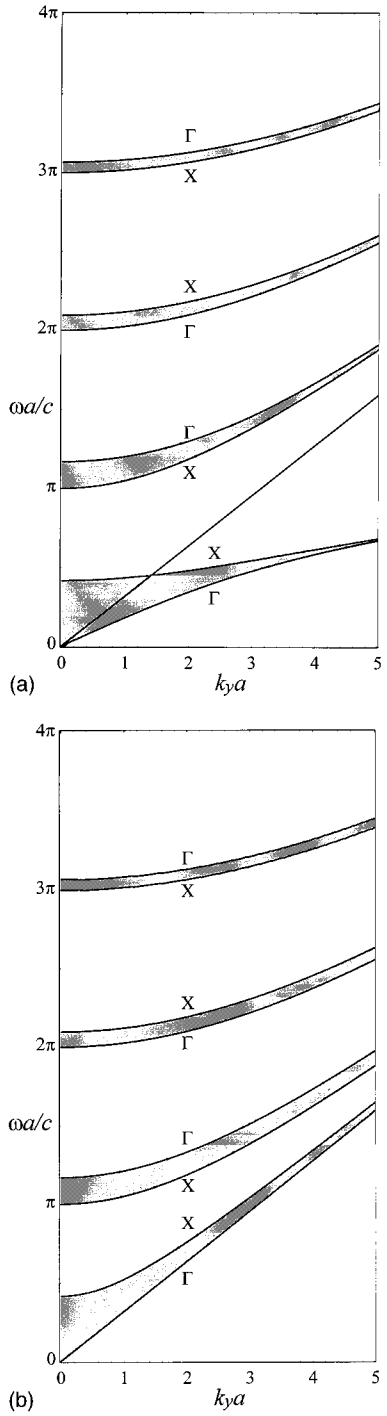

FIG. 5. Bands of dispersion curves (shown shaded) ω vs the transverse wave-vector component k_y, for a periodic one-dimensional array of infinitesimal sheets: (a) s polarization, with the light line $\omega=ck_y$ included, and (b) p polarization. The modes are locally propagating except for the locally evanescent solutions to the right of the light line in (a).

II B shows that the single dielectric sheet supports waveguide modes with s polarization, and the associated evanescent fields fall off on either side of the sheet with a characteristic range $1/q$, where q is given by Eq. (2.24). We accordingly expect the one-dimensional lattice to have analogous modes and we seek locally evanescent solutions in which the local wave vector k_x is imaginary, and conveniently replaced by iq_x, so that the wave-vector-frequency relation (2.10) takes the form of Eq. (2.14). The calculations outlined in Sec. III A remain valid with the changed nature of the wave vector and the s-polarization dispersion relation (3.7) is converted to

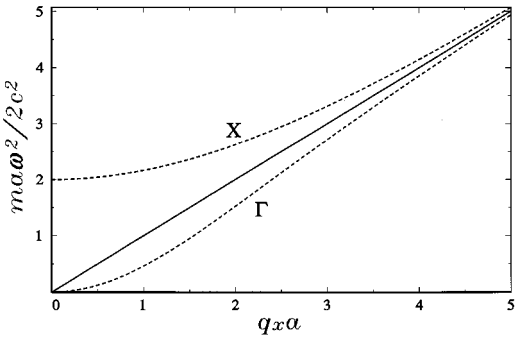

FIG. 6. Variation of ω^2 with the local wave vector q_x for the evanescent modes of a one-dimensional array of infinitesimal sheets. The broken lines show the exact solutions (3.16) and (3.17), while the continuous line shows the approximate solution $q_x=q$.

$$\cos(\mu_x a)=\cosh(q_x a)-(m\omega^2/2c^2q_x)\sinh(q_x a). \qquad (3.15)$$

It is emphasized that the Bloch waves continue to have propagating characters, despite their formation from locally evanescent electromagnetic-field distributions.

The broken lines in Fig. 4 show some constant-frequency contours obtained by the solution of Eq. (3.15) with the use of Eq. (2.14). The evanescent modes are characterized by a transverse wave-vector component k_y greater than ω/c. Some of the contours change character from locally propagating to locally evanescent as k_x changes from real to imaginary, and it is clear from Eqs. (2.10) or (2.14) that the changeover occurs at glancing incidence when $k_x=0$ or $k_y=\omega/c$. The reflection coefficient for s polarization given by Eq. (2.8) takes the value $r_s=-1$ at the changeover point, so that the incident and reflected electric fields interfere destructively to give zero total field.

The dispersion relation again simplifies at the symmetry points, but there is now only one kind of solution at each. Thus the solution of Eq. (3.15) at Γ is

$$\tanh(q_x a/2)=m\omega^2/2c^2q_x \quad (\mu_x=0) \qquad (3.16)$$

and that at X is

$$\coth(q_x a/2)=m\omega^2/2c^2q_x \quad (\mu_x=\pi/a). \qquad (3.17)$$

The broken lines in Fig. 6 show the variations of ω^2 with q_x obtained from these solutions. The same waveguide solutions appear in a different guise in the part of Fig. 5(a) to the right of the light line where $k_y>\omega/c$.

We note that there are no evanescent solutions for p polarization in the absence of any analogous guided waves in the single sheet, although excitations with $k_y>\omega/c$ do exist for an array of finite-thickness dielectric slabs [19].

The waveguide modes in the individual sheets that form the one-dimensional array can be considered as tightly bound when

$$qa = ma\omega^2/2c^2 \gg 1, \tag{3.18}$$

where Eq. (2.24) has been used. In this regime we expect that the waveguide modes in a single sheet are only slightly affected by the presence of adjacent sheets in the array. When the inequality (3.18) is satisfied, the solutions (3.16) and (3.17) for q_x both tend to q, similar to Eq. (2.24), and this approximate solution is shown by the continuous line in Fig. 6. More generally $q_x = q$ is an approximate solution of Eq. (3.15) irrespective of the magnitude of the Bloch wave vector μ_x. This dispersion relation can be rearranged with the help of Eq. (2.14) in the form

$$\frac{\omega}{c} = \left(\frac{(1+m^2k_y^2)^{1/2}-1}{m^2/2} \right)^{1/2}, \tag{3.19}$$

which is identical to Eq. (2.25). The evanescent waveguide modes of the individual dielectric sheets thus combine in the tight-binding limit (3.18) to produce propagating Bloch waves of the one-dimensional array of sheets. The frequencies of these modes are independent of the Bloch wave vector μ_x in conditions where the inequality (3.18) is satisfied.

It is also straightforward to show that in the limit given by Eq. (3.18), the two amplitudes in Eq. (3.2) have the simple ratio

$$E_n^+/E_n^- = e^{(2n-1)qa - i\mu_x a}. \tag{3.20}$$

Hence, in terms of the amplitude E_0^- in the zeroth cell, the electric field takes the form

$$\mathbf{E}(\mathbf{r}) = \hat{\mathbf{z}} E_0^- e^{ik_y y + i\mu_x x} \{ e^{-i\mu_x (x-na)} [e^{-q(x-(n-1)a) - i\mu_x a} + e^{q(x-na)}] \} \quad \text{for } (n-1)a < x < na. \tag{3.21}$$

It is seen that the field in this expression explicitly satisfies Bloch's theorem (3.4); the term in the outer braces is periodic in the lattice constant a. As the field around each sheet decays rapidly, Eq. (3.21) may be written in the approximate form

$$\mathbf{E}(\mathbf{r}) = \hat{\mathbf{z}} E_0^- e^{ik_y y} \sum_{n=-\infty}^{\infty} e^{i\mu_x na} \psi(x-na), \tag{3.22}$$

where

$$\psi(x) = e^{-q_0|x|} \tag{3.23}$$

is the form of the wave function around a *single* sheet in this limit. Eq. (3.22) is precisely the ansatz for the tight-binding method, often used in band structure calculations [21], in which the multiatom wave function is approximated by a combination of single-atom wave functions in a manner similar to that given in Eq. (3.22).

IV. TWO-DIMENSIONAL LATTICE

We consider in this section the photonic band structure in an infinite lattice formed from two identical arrays of infinitesimal dielectric sheets at right angles. The x and y axes are taken as the normals to the sheets, which have indefinite extents in the direction of the z axis. The array of sheets with period a is specified by the dielectric function

$$\varepsilon(\mathbf{r}) = 1 + m \left\{ \sum_{n_x=-\infty}^{\infty} \delta(x - n_x a) + \sum_{n_y=-\infty}^{\infty} \delta(y - n_y a) \right\}. \tag{4.1}$$

The primitive cell is thus an infinite prism whose cross section is a square of side a, and the symmetry of the lattice corresponds to the point group $4/mmm$ or D_{4h}. The spatial arrangement of the lattice is shown in Fig. 7.

The lattice defined above is three dimensional, but the calculations presented here assume propagation parallel to the xy plane with a local wave vector $\mathbf{k} = (k_x, k_y)$ whose components again satisfy Eq. (2.10). The corresponding wave-vector space is thus two dimensional. The Bloch wave vector is denoted $\boldsymbol{\mu} = (\mu_x, \mu_y)$ and the associated two-dimensional Brillouin zone of the lattice defined by Eq. (4.1) covers the range

$$-\pi/a < \mu_x, \mu_y < \pi/a. \tag{4.2}$$

Figure 8 shows one quadrant of the Brillouin zone with the conventional notation [22] for its points and lines of high symmetry.

A. Locally propagating modes

For a propagation wave vector parallel to the xy plane, the fields continue to decompose into s polarization (**E** parallel to z) and p polarization (**E** parallel to the xy plane), and these polarization characters are identical with respect to the two sets of sheets that form the lattice.

For s polarization, the electric field in a primitive cell specified by indices n_x and n_y takes the form

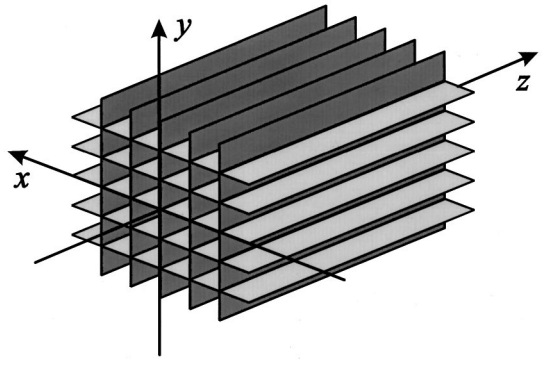

FIG. 7. Geometrical arrangement of the two-dimensional lattice.

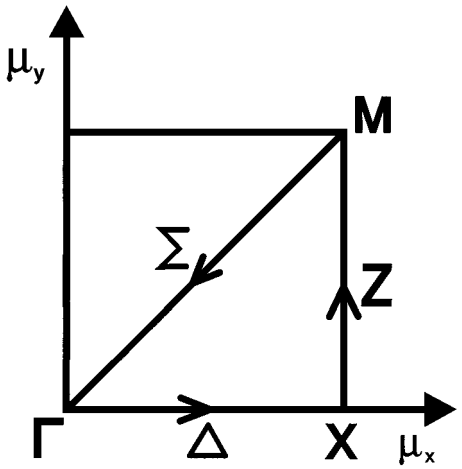

FIG. 8. Quadrant of the Brillouin zone of the square two-dimensional lattice showing the notation for symmetry points and lines.

$$\mathbf{E}(\mathbf{r})=\hat{\mathbf{z}}E_{n_x,n_y}(\mathbf{r})$$

$$=\hat{\mathbf{z}}\{E^{+}_{n_x}e^{ik_x x}+E^{-}_{n_x}e^{-ik_x x}\}\{E^{+}_{n_y}e^{ik_y y}+E^{-}_{n_y}e^{-ik_y y}\}$$

$$\text{for } (n_x-1)a<x<n_x a, \quad (n_y-1)a<y<n_y a, \tag{4.3}$$

which is a generalization of the locally propagating field (3.2) in a one-dimensional lattice. The corresponding magnetic field is obtained from the $\nabla\times\mathbf{E}$ Maxwell equation, and the relations between the fields in adjacent primitive cells in the xy plane are obtained by application of the boundary conditions (2.2)–(2.5). This procedure can be applied separately to the adjacent cells in the x and y directions. It is evident from Eq. (4.3) that the field in each cell is described by a four-component vector of field amplitudes, as compared with the two components in Eq. (3.2). The extra components, however, describe propagation by an additional pair of waves with negative-going wave-vector y components, which do not couple to the first pair. As a result, the associated (4×4) transfer matrix block diagonalizes to two (2×2) matrices of the form shown in Eq. (3.3), and the connections are the same as found for the one-dimensional lattice. Bloch's theorem also separates into two relations equivalent to Eq. (3.4). The two-dimensional calculation therefore results in a pair of relations similar to Eq. (3.7),

$$\cos(\mu_x a)=\cos(k_x a)-(mk^2/2k_x)\sin(k_x a)$$

$$\cos(\mu_y a)=\cos(k_y a)-(mk^2/2k_y)\sin(k_y a) \tag{4.4}$$

and the dispersion relation, ω versus μ, is obtained by solution of these equations subject to the constraint (2.10).

A very similar analysis, with the electric field $\mathbf{E}$ in Eq. (4.3) replaced by the z component of the magnetic field $\mathbf{H}$, can be used for p polarization, and the dispersion relations are obtained by solution of the pair of equations

$$\cos(\mu_x a)=\cos(k_x a)-\tfrac{1}{2}mk_x\sin(k_x a),$$

$$\cos(\mu_y a)=\cos(k_y a)-\tfrac{1}{2}mk_y\sin(k_y a), \tag{4.5}$$

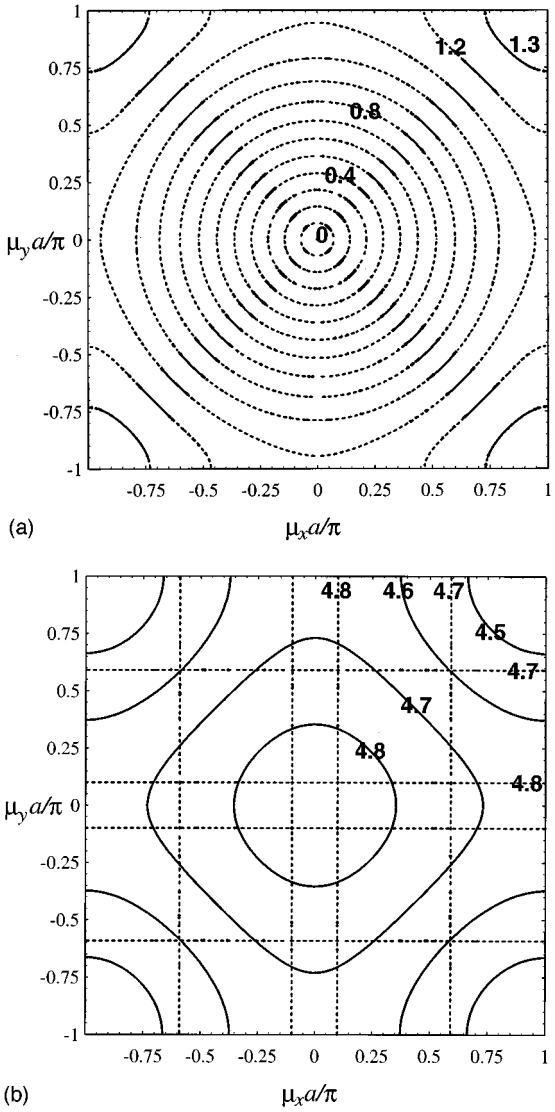

FIG. 9. Constant-frequency contours in the complete Brillouin zone for modes with s polarization in a two-dimensional array of infinitesimal sheets with $m=2a$. The continuous lines show locally propagating solutions and the broken lines show locally evanescent solutions. The numbers attached to the curves show the values of $\omega a/c$, which cover the ranges (a) 0–1.3 and (b) 4.5–4.8.

similar to Eq. (3.10), and again subject to the constraint (2.10).

It is instructive to display the behavior of the modes by contour diagrams, similar to Fig. 4 for the one-dimensional lattice. Several of these have already been presented and discussed [16], and we concentrate here on the more interesting behavior of the s-polarized modes. Constant-frequency contours are obtained by parametrizing the local wave vector $\mathbf{k}$ in Eqs. (4.4) and (4.5) as

$$k_x=(\omega/c)\cos\theta, \quad k_y=(\omega/c)\sin\theta, \quad k_z=0, \tag{4.6}$$

which clearly satisfies Eq. (2.10) and represents a traveling local wave. Points (μ_x,μ_y) are then computed from Eqs. (4.4) or (4.5) for constant ω as θ is varied from 0 to $\pi/2$. Figure 9 shows such contours for s polarization, with $m=2a$, and for two ranges of the frequency. Only the con-

tinuous parts of the contours result from the locally propagating fields and it is seen in the low-frequency regime of Fig. 9(a) that these extend only slightly on either side of the zone diagonals Σ, for which $\mu_x=\mu_y$. It is clear from Eq. (4.4) that μ_x does not vanish when $k_x=0$, and similarly μ_y with k_y, and the extremes of each continuous portion of contour thus correspond to local wave vectors aligned parallel to one set of dielectric sheets. We note that this phenomenon does not occur for p polarization, where all the Bloch excitations are associated with propagating local fields. The broken sections of the s-polarization contours are associated with evanescent local waves, and these are discussed in Sec. IV B. Successive bands for higher frequencies ($\omega a/c>1.3$) are derived completely from evanescent local waves, up to one of the bands whose contours are shown in Fig. 9(b). Two types of band coexist at these frequencies, one derived from evanescent local waves, with almost straight contours, and the other derived from propagating local waves.

The constant-frequency curves can be translated into the more conventional dispersion curves by projection onto the appropriate μ-space direction: $\mu_y=0$ for the Δ or ΓX direction, $\mu_x a=\pi$ for Z or XM and $\mu_x=\mu_y$ for Σ or $M\Gamma$. The p-polarization dispersion curves for the first two directions have the useful property that they can be computed initially in a frequency-independent fashion. Thus with μ_y set equal to zero in Eq. (4.5) and $k_y\leqslant\omega/c$ the alternative conditions

$$\sin(k_y a/2)=0 \quad \text{or} \quad -(mk_y/2)\cos(k_y a/2) \tag{4.7}$$

are obtained. These equations effectively ''quantize'' the allowed values of k_y, whereas the corresponding one-dimensional lattice periodic in the x direction, treated in Sec. III, has a continuous range of available values of k_y. The resulting bands for the ΓX direction are now obtained from the first equation of Eq. (4.5),

$$\cos(\mu_x a)=\cos\sqrt{(\omega a/c)^2-(k_y a)^2} - \tfrac{1}{2}m\sqrt{(\omega/c)^2-k_y^2}\,\sin\sqrt{(\omega a/c)^2-(k_y a)^2}. \tag{4.8}$$

Each solution of Eq. (4.7) thus generates a family of bands extending up the frequency axis from a minimum value determined by the condition $\omega\geqslant ck_y$. A similar general method pertains to the XM direction, but the condition $\mu_x=\mu_y$ for the $M\Gamma$ direction provides no general frequency-independent route to the dispersion curves. Neither does there exist a simplification in any direction for s polarization. For these curves, the relevant value of μ_x or μ_y must be found by direct solution of the transcendental equations (4.4) or (4.5) for each value of ω.

The resulting dispersion curves for $m=2a$ are shown by the continuous lines in Fig. 10. These include all of the curves for p polarization shown in Fig. 10(b), but for s polarization only the low-frequency band in the Σ or $M\Gamma$ direction and the continuous curve near the top of Fig. 10(a) correspond to Bloch waves formed from locally propagating fields. These two bands are associated with the continuous contours in Figs. 9(a) and 9(b), respectively. It is seen that for s polarization there are also many bands associated with locally evanescent fields, indicated by broken lines, and

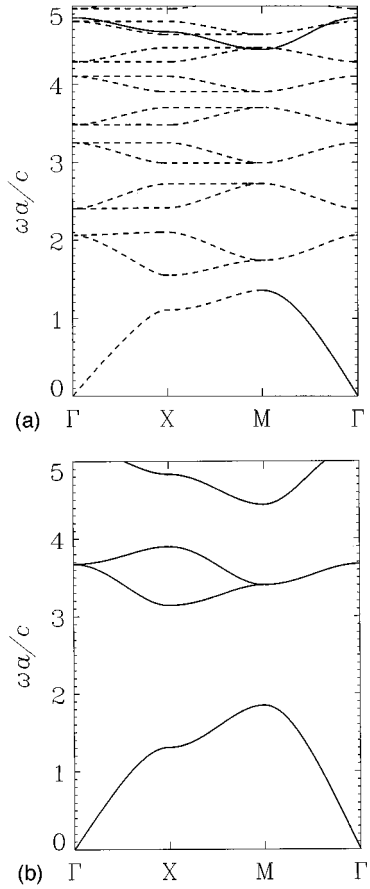

FIG. 10. Dispersion relations, ω vs the Bloch wave vector μ, for a two-dimensional lattice with $m=2a$ showing (a) s polarization and (b) p polarization. The continuous lines show locally propagating solutions and the broken lines show locally evanescent solutions.

these are considered in Sec. IV B. The solutions are nondegenerate in the ΓX and XM directions but many of the modes have twofold degeneracy for Bloch wave vectors with $\mu_x=\mu_y$ in the $M\Gamma$ direction, including the symmetry points Γ and M at the ends of the line. The degeneracy is a direct consequence of the symmetry between μ_x and μ_y in Eqs. (4.4) and (4.5). These equations have some simple solutions at symmetry points in the Brillouin zone, similar to Eqs. (3.11) and (3.13), that are independent of the value of m. Thus there are fixed values of $\omega a/c$ equal to $\sqrt{2}\pi$ at symmetry point M for both s and p polarizations and equal to π at point X for p polarization. These fixed frequencies, independent of m, occur in regular progressions up the series of photonic bands beyond those shown in the restricted range of Fig. 10.

The long-wavelength behavior of the propagating-mode dispersion relations is readily obtained by expansions of Eqs. (4.4) and (4.5) for small values of the Bloch wave-vector components. Thus for s polarization, we find from Eq. (4.4) with the use of Eq. (2.10) that

$$\mu^2 a^2=(\mu_x^2+\mu_y^2)a^2\approx\frac{a^2\omega^2}{c^2}\left(1+\frac{2m}{a}\right) \quad \text{for } \mu a\ll 1, \tag{4.9}$$

and the long-wavelength dispersion relation is

$$\omega=\frac{\mu c}{[1+(2m/a)]^{1/2}}. \tag{4.10}$$

The quantity $[1+(2m/a)]^{1/2}$ plays the role of the effective low-frequency refractive index, and it is seen from Eq. (2.1) that $1+(2m/a)$ is indeed the average relative permittivity of the two-dimensional lattice. Similarly for p polarization, the long-wavelength dispersion relation obtained from Eq. (4.5) with the use of Eq. (2.10) is

$$\omega=\frac{\mu c}{[1+(m/a)]^{1/2}}. \tag{4.11}$$

The smaller effective refractive index $[1+(m/a)]^{1/2}$ for p polarization reflects the reduced average values of the electric field inside the dielectric sheets. Thus, given the continuity of the field components parallel to the surfaces but the zero normal components of the electric fields inside the sheets, $1+(m/a)$ is the energy-weighted value of the relative permittivity [3,15] when this is averaged over all directions of propagation. Effective refractive indices for general values of the wavelength in photonic band gap materials have been considered by Dowling and Bowden [23].

B. Locally evanescent modes

A striking feature of the band structure for s-polarized radiation, as demonstrated in Figs. 9(a) and 10(a), is the predominance of Bloch modes arising from locally evanescent fields. The constant-frequency contours can be obtained by a replacement of the propagating wave-vector parametrization in Eq. (4.6) by the hyperbolic form

$$k_x\equiv iq_x=i(\omega/c)\sinh\varphi,\quad k_y=(\omega/c)\cosh\varphi,\quad k_z=0, \tag{4.12}$$

where φ ranges from 0 to ∞. Here the x dependence of the local field is taken to have evanescent character, where k_x may be replaced by iq_x, and the y dependence retains a propagating form with $k_y>\omega/c$, so that Eq. (2.14) is satisfied. The broken contours in Fig. 9(a) are generated by this parameterization, together with an alternative scheme in which k_x and k_y are interchanged. The broken curves in Fig. 10(a) also signify locally evanescent modes and these account for most of the Bloch wave propagation over the frequency range shown.

The regularity of the broken bands in Fig. 10(a) suggests a common cause and we seek a simple physical explanation. Similar to the discussion of Sec. III B, we look for approximate solutions of the relations (4.4) for s polarization in conditions where the inequality (3.15) holds and the waveguide modes of the single sheets are expected to be only slightly perturbed by their formation into a two-dimensional lattice.

Suppose first, as in Eq. (4.12), that the x dependences of the fields on both sides of a sheet have evanescent characters, while the y dependences of the fields retain propagating forms. The first equation in the pair (4.4) is converted to

$$\cos(\mu_x a)=\cosh(q_x a)-(m\omega^2/2c^2q_x)\sinh(q_x a), \tag{4.13}$$

identical in form to Eq. (3.15), and in the tight-binding regime, where $q_x a\gg 1$, this has the approximate solution

$$q_x=m\omega^2/2c^2, \tag{4.14}$$

irrespective of the value of μ_x. It follows from Eq. (2.14) that

$$k_y=\frac{\omega}{c}\left(\frac{m^2\omega^2}{4c^2}+1\right)^{1/2}\approx\frac{m\omega^2}{2c^2}+\frac{1}{m}, \tag{4.15}$$

where the first equality is equivalent to the single-sheet dispersion relation (2.25). The approximate form is valid when the inequality (3.18) is satisfied and in addition m is of the order of the lattice constant a or greater. This approximation may now be inserted in the second of the pair of equations (4.4); only the much larger first term on the right-hand side of Eq. (4.15) need be retained in the prefactor of the sine function, but both terms must be kept within the trigonometric functions since a/m may be significant relative to 2π. Thus the second equation of Eq. (4.4) becomes

$$\begin{aligned}\cos(\mu_y a)&=\cos\left(\frac{ma\omega^2}{2c^2}+\frac{a}{m}\right)-\sin\left(\frac{ma\omega^2}{2c^2}+\frac{a}{m}\right)\\&=\sqrt{2}\,\cos\left(\frac{ma\omega^2}{2c^2}+\frac{a}{m}+\frac{\pi}{4}\right),\end{aligned} \tag{4.16}$$

with solutions

$$\omega^2=\frac{2c^2}{ma}\left\{(2n-\tfrac{1}{4})\pi-\frac{a}{m}\pm\cos^{-1}\left(\frac{\cos(\mu_y a)}{\sqrt{2}}\right)\right\},\qquad n=1,2,3,\ldots, \tag{4.17}$$

that are independent of the x component of the Bloch wave vector. Some examples are shown by the horizontal broken lines in Fig. 9(b).

Similarly, if the x dependences of the fields have propagating characters but their y dependences are evanescent, the analysis is the same as in Eqs. (4.13) to (4.16) and the approximate dispersion relation is

$$\cos(\mu_x a)=\sqrt{2}\,\cos\left(\frac{ma\omega^2}{2c^2}+\frac{a}{m}+\frac{\pi}{4}\right), \tag{4.18}$$

with solutions

$$\omega^2=\frac{2c^2}{ma}\left\{(2n-\tfrac{1}{4})\pi-\frac{a}{m}\pm\cos^{-1}\left(\frac{\cos(\mu_x a)}{\sqrt{2}}\right)\right\},\qquad n=1,2,3,\ldots, \tag{4.19}$$

that are independent of the y component of the Bloch wave vector. Some examples are shown by the vertical broken lines in Fig. 9(b).

The dispersion relations (4.17) and (4.19) provide four distinct bands for each choice of n when account is taken of the choice of sign in each. These four bands form into two overlapping pairs separated by a gap; the lower-frequency pair for each n covers the range from

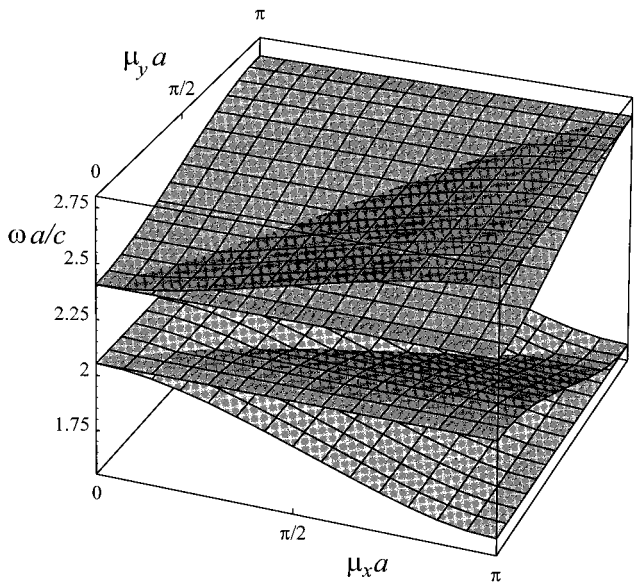

FIG. 11. Dispersion surfaces ω vs the Bloch wave vector μ, over a quadrant of the Brillouin zone for the $n=1$ quartet of locally evanescent bands in a two-dimensional lattice with $m=2a$.

$$\frac{\omega a}{c}=\left[\frac{2a}{m}\left(2n\pi-\pi-\frac{a}{m}\right)\right]^{1/2} \text{ to } \left[\frac{2a}{m}\left(2n\pi-\frac{\pi}{2}-\frac{a}{m}\right)\right]^{1/2}, \tag{4.20}$$

while the higher-frequency pair covers the range from

$$\frac{\omega a}{c}=\left[\frac{2a}{m}\left(2n\pi-\frac{a}{m}\right)\right]^{1/2} \text{ to } \left[\frac{2a}{m}\left(2n\pi+\frac{\pi}{2}-\frac{a}{m}\right)\right]^{1/2}. \tag{4.21}$$

Figure 11 shows the set of dispersion surfaces for $n=1$, and the sets for higher values of n are essentially the same, except that the presence of ω^2 on the left-hand sides of the dispersion relations leads to a compression of the bands with increasing frequency when they are plotted against a linear ω axis.

These features of the tight-binding bands are clearly visible in the dispersion curves for s polarization in Fig. 10(a), where most of the curves are grouped in repeating patterns of four bands. For the choice of quadrant shown in Fig. 8, the flat bands on the symmetry line Δ or ΓX are provided by the dispersion relations (4.17) with the two choices of sign, while the curved bands are provided by the dispersion relations (4.19), and these roles are reversed on the symmetry line Z or XM. The twofold degeneracies on the line Σ or $M\Gamma$ are obvious consequences of the crossings of pairs of dispersion sheets obtained from Eqs. (4.17) and (4.19). Only the lowest pair of bands in Fig. 10(a), belonging to the $n=1$ contribution to the pattern, show significant departures from their approximate tight-binding forms, and this should be expected since with $\omega a/c\approx 2$ and $m=2a$, the inequality in Eq. (3.18) is poorly satisfied. Note that, unlike the Bloch waves formed from locally propagating fields, there are no fixed values of $\omega a/c$, independent of m, for the Bloch waves formed from locally evanescent fields.

The lowest band in Fig. 10(a), extending down to zero frequency, and the band shown by the continuous curve near the top of the figure do not belong to the fourfold units characteristic of the tightly bound locally evanescent modes. Thus the inequality (3.18) clearly does not apply to the lowest band, which is everywhere nondegenerate, and takes locally propagating or locally evanescent characters depending on the direction of the Bloch wave vector. The band near the top of Fig. 10(a) corresponds everywhere to Bloch waves formed from locally propagating fields. The expansions of Eq. (4.13) and the second equation in the pair Eq. (4.4) for small values of the Bloch wave-vector components lead, with the use of Eq. (2.14), to the same low-frequency dispersion relation for the locally evanescent modes as obtained in Eq. (4.10) for the locally propagating modes.

C. Density of states

The density of modes in the photonic bands is an important function in the determination of the optical and thermodynamic properties of the lattice. Adaptation of the conventional definition to the two-dimensional Brillouin zone used here gives the expression

$$\rho(\omega)=(2\pi)^{-2}\sum_b \int d^2\mu\,\delta(\omega-\omega_b(\boldsymbol{\mu})) \tag{4.22}$$

for the density of states per unit frequency range per unit area of lattice. Here $\omega_b(\boldsymbol{\mu})$ is the frequency of the photonic band labeled b at the Bloch wave vector $\boldsymbol{\mu}$, and the summation and integration run over all bands and wave vectors, respectively.

Figure 12 shows the densities of states for the s- and p-polarized modes as functions of the frequency calculated numerically from the dispersion relations (4.4), (4.5), and (4.13). The curves show critical-point singularities associated with the symmetry points in the Brillouin zone. Consider first the density of states for p polarization shown in Fig. 12(b). The contribution of the lowest-frequency band shows an initial linear dependence on the frequency, associated with the linear dispersion (4.11) close to the Γ point, a logarithmic singularity associated with the saddle at point X, and a vertical step associated with the maximum in the dispersion curves at point M. The contribution of the second band shows vertical steps associated with the minimum and maximum at point X, and logarithmic singularities associated with the saddles at points Γ and X. These steps and singularities are characteristic features of densities of states in two-dimensional systems. The density of states for s polarization shown in Fig. 12(a) includes some similar features, but the distribution is dominated by the additional contributions of the locally evanescent modes, shown by the broken curves. The frequencies of these modes vary with only a single Bloch vector component in the tight-binding regime, and their contributions to the density of states tend, with increasing frequency, towards one-dimensional forms with very sharp inverse square-root singularities at their maxima and minima. Comparison of the two parts of Fig. 12 shows that there are substantially more states for s polarization than for p polarization.

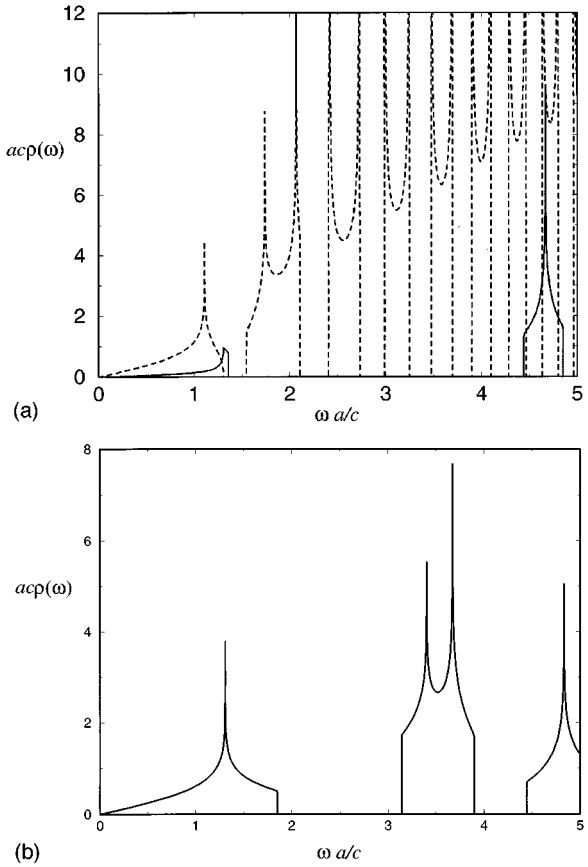

FIG. 12. Density-of-states functions for the photonic bands illustrated in Fig. 9 showing (a) s polarization and (b) p polarization. For s polarization, the continuous lines indicate the contributions of modes for which the local wave vector is real, while the broken lines indicate contributions for which one component of the local wave vector is imaginary. For p polarization, all of the modes have real local wave vectors.

The repeating pattern in the density of states for s polarization is contributed by the succession of locally evanescent dispersion surfaces of the kind illustrated in Fig. 11, and this contribution can be calculated analytically in the tight-binding limit using the dispersion relations derived above. Thus the frequencies for insertion as $\omega_b(\boldsymbol{\mu})$ in Eq. (4.22) are obtained from Eqs. (4.17) and (4.19) and only two dispersion surfaces contribute for any value of ω. The δ function in Eq. (4.22) involves only a single Bloch wave-vector component, as $\omega_b(\boldsymbol{\mu})$ is independent of either μ_x or μ_y, and in order to perform the corresponding integral we need to convert this δ-function by the usual procedure, using

$$\frac{\partial}{\partial\mu_i}[\omega-\omega_b(\mu_i)]=\mp\left(\frac{ac^2}{2m}\right)^{1/2}\frac{\sin(\mu_i a)}{[2-\cos^2(\mu_i a)]^{1/2}}\times\left\{(2n-\tfrac{1}{4})\pi-\frac{a}{m}\pm\cos^{-1}\left(\frac{\cos(\mu_i a)}{\sqrt{2}}\right)\right\}^{-1/2}, \quad (4.23)$$

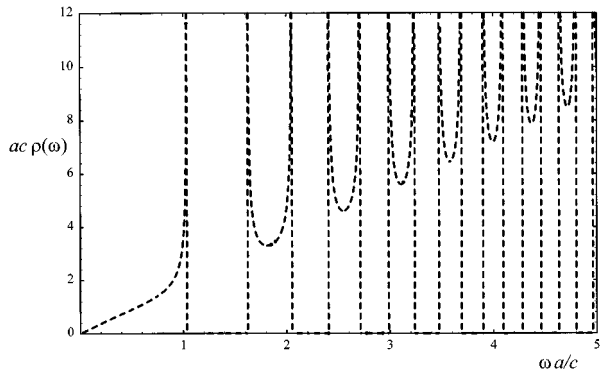

FIG. 13. Density of states for the tight-binding s-polarized modes calculated from Eq. (4.25).

where $i=x$ or y. Evaluation of this expression at the wave-vector components that satisfy the dispersion relation (4.17) or (4.19) leads with the use of Eq. (4.16) to

$$\left|\frac{\partial}{\partial\mu_i}[\omega-\omega_b(\mu_i)]\right|=\frac{c^2}{\sqrt{2}m\omega}\left|\frac{\sin^{1/2}\left(\frac{ma\omega^2}{c^2}+\frac{2a}{m}\right)}{\sin\left(\frac{ma\omega^2}{2c^2}+\frac{a}{m}+\frac{\pi}{4}\right)}\right|. \quad (4.24)$$

The density of states (4.22) therefore takes the form

$$\rho(\omega)=\frac{2\sqrt{2}m\omega}{\pi ac^2}\left|\frac{\sin\left(\frac{ma\omega^2}{2c^2}+\frac{a}{m}+\frac{\pi}{4}\right)}{\sin^{1/2}\left(\frac{ma\omega^2}{c^2}+\frac{2a}{m}\right)}\right|, \quad (4.25)$$

where an additional factor of 2 results from the two values $\pm\mu_i$ of the Bloch wave-vector component for each value of ω. This function is shown in Fig. 13, and it is seen that there is good agreement with the exact calculation in Fig. 12(a) from the third band onward, where the tight-binding approximation is justified for the assumed value of $m=2a$. The argument of the sine in the denominator of Eq. (4.25) vanishes at all of the band-edge frequencies given in Eqs. (4.20) and (4.21), and the density of states thus acquires inverse square-root singularities of the form

$$\rho(\omega)=\frac{1}{\pi ac}\left(\frac{2m\omega_0}{a|\omega-\omega_0|}\right)^{1/2}, \quad (4.26)$$

where ω_0 is the appropriate adjacent band-edge frequency.

The contribution to the density of states from each pair of overlapping bands has the same integrated value, which is straightforwardly obtained from Eq. (4.25) with the use of Eqs. (4.20) and (4.21), by a suitable change of variable, as

$$\int_{\text{band}}d\omega\ \rho(\omega)=\frac{2\sqrt{2}}{\pi a^2}\int_0^{\pi/2}du\ \frac{\sin\left(u+\frac{\pi}{4}\right)}{\sin^{1/2}(2u)}=\frac{2\sqrt{2}}{\pi a^2}\int_0^{\pi/2}du(\tan u)^{1/2}=\frac{2}{a^2}, \quad (4.27)$$

where a standard integral has been used [24]. This result agrees with the value obtained for the total density of states in a pair of bands by straightforward integration of Eq. (4.22) over ω. The overall density of states of the tightly bound locally evanescent modes can be assessed by forming a smoothed average of their contributions. Thus the repeating patterns of four bands occur approximately at frequencies given by Eqs. (4.20) and (4.21) as

$$\omega = c\left(\frac{4\pi n}{am}\right)^{1/2}. \tag{4.28}$$

The separation between these frequencies is

$$\Delta\omega \approx c\left(\frac{\pi}{amn}\right)^{1/2} = \frac{2\pi c^2}{ma\omega}, \tag{4.29}$$

since $\Delta n = 1$, and the smoothed density of states is therefore

$$\rho(\omega) = \frac{4}{a^2\Delta\omega} = \frac{2m\omega}{\pi a c^2}. \tag{4.30}$$

For comparison, the density of states for each polarization in a two-dimensional space entirely filled with a material of relative permittivity ε is

$$\rho(\omega) = \omega\varepsilon/2\pi c^2, \tag{4.31}$$

and the multiplicative factor $4m/a$ in Eq. (4.30) relative to the density of states in free space thus accounts for the additional density of states provided by the dielectric material for both polarizations.

That all of the additional density of states should appear in *s* polarization and none in *p* polarization is a consequence of the restriction of the single-sheet guided-wave modes to *s* polarization, as discussed in Sec. II B. A superficial comparison of the two parts of Fig. 12 thus gives the impression that there are more modes with *s* polarization than with *p* polarization, but this is misleading. The number of independent modes in each extended Brillouin zone of a periodic system is equal to the number N of unit cells in the sample. Thus in the reduced zone scheme, each band must contain N states, which correspond to the allowed wave vectors, and the total numbers of states are the same for each polarization. The relative permittivity in any real material is a function of the frequency, $\varepsilon(\omega)$, and it satisfies the sum rule [25]

$$\int_0^\infty d\omega[\mathrm{Re}\varepsilon(\omega) - 1] = 0, \tag{4.32}$$

provided that $\varepsilon(\omega)$ has no pole at $\omega = 0$. The enhancement of the density of states (4.31), for regions of the frequency where $\varepsilon(\omega)$ is greater than unity, is therefore compensated by other regions of the frequency, where $\varepsilon(\omega)$ is smaller than unity. The dispersion curves shown in Fig. 10 and the densities of states shown in Fig. 12 are valid over a limited range of frequencies in which the value of $\varepsilon(\omega)$ is assumed essentially constant. However, a more extended range of calculation, with a properly frequency dependent $\varepsilon(\omega)$, would show a reduction in the number of *s* polarized modes at higher frequencies in accordance with Eqs. (4.31) and (4.32), to give the same total numbers of modes for both polarizations.

The remaining features in the densities of states shown in Fig. 12 are associated with the locally propagating modes or the mixed propagating-evanescent modes. The linear contributions at low frequency for both polarizations have the magnitudes predicted by Eq. (4.31) when ε is replaced by the averaged relative permittivities that appear in the square roots in the long-wavelength linear dispersion relations derived in Eqs. (4.10) and (4.11). The locally propagating contributions for *s* polarization and all of the *p* polarization density of states retain the characteristic two-dimensional critical-point singularities at the higher frequencies illustrated, in contrast to the one-dimensional characters of the locally evanescent contributions.

The contributions of the locally propagating and locally evanescent waves to the densities of states show quite different behaviors as m is increased from its empty-lattice or free-space value of 0. Thus the existence of fixed values of $\omega a/c$, independent of m, for selected points on the locally propagating dispersion curves, mentioned in Sec. IV A, ensures that the overall distribution of their density of states shows only modest changes as m is increased. By contrast, the lack of any fixed values of $\omega a/c$ on the locally evanescent dispersion curves, mentioned in Sec. IV B, allows large changes in their density of states as m is increased. This freedom permits the density of states (4.30) to grow linearly with m as the frequencies of the locally evanescent Bloch waves diminish in accordance with Eq. (4.28), and it leads to the apparent excess density of states in *s* polarization for the limited ranges of frequency shown in Figs. 10 and 12.

It is seen from Fig. 12 that three gaps appear in the combined density of states in the range of frequencies covered. The ranges of $\omega a/c$, for which there are no photonic modes of the lattice, are found with the use of Eqs. (4.20) and (4.21) to be

$$\left(\frac{3\pi}{2} - \frac{1}{2}\right)^{1/2} \text{ to } \left(2\pi - \frac{1}{2}\right)^{1/2},$$

$$\left(\frac{5\pi}{2} - \frac{1}{2}\right)^{1/2} \text{ to } \left(3\pi - \frac{1}{2}\right)^{1/2},$$

$$\left(\frac{11\pi}{2} - \frac{1}{2}\right)^{1/2} \text{ to } \left(6\pi - \frac{1}{2}\right)^{1/2}. \tag{4.33}$$

The dispositions of gaps in the density of states are important for applications to semiconductor lasers, as they produce quenching of the spontaneous emission over the corresponding transition frequencies. It should be emphasized, however, that the gaps identified here are valid only for propagation in the xy plane and that the addition of z components of the wave vector may lead to photon modes within these gaps.

V. CONCLUSIONS

We have calculated the photonic properties of a single dielectric sheet, a one-dimensional lattice of such sheets, and a two-dimensional square lattice of the same sheets, in the limit where the sheet thickness tends to zero as its relative permittivity tends to infinity. Although these lattices cannot be constructed in practice, their properties resemble those of structures with appropriately thin slabs of high relative per-

mittivity, and they have the advantage that their photonic properties can be evaluated analytically to a large extent. The analytical treatment provides a more detailed physical understanding of the natures of the photonic Bloch waves in such structures.

We have accordingly identified the separation of the Bloch waves into two distinct categories. Thus a few of the waves for s polarization and all of the waves for p polarization are constructed from fields with locally propagating characters in the individual primitive cells of the lattice, whereas the majority of the Bloch waves for s polarization are formed from fields with locally evanescent characters in the individual primitive cells. The latter waves are in turn associated with the waveguide modes of the dielectric sheets, which thus dominate the low-frequency photonic band structure and density of states of the two-dimensional lattice for waves of s polarization. The locally evanescent photonic bands are assembled from a stack of the basic building blocks illustrated in Fig. 11 and these give a characteristic repeating pattern to the band structure for s polarization illustrated in Fig. 10(a). The corresponding contributions to the density of states also form a repeating pattern as illustrated in Figs. 12(a) and 13. We have shown that the locally evanescent modes enhance the photonic density of states above its free-space value when $4m > a$, but that this is compensated by reductions below the free-space value that occur for $4m < a$ in real dielectric materials, where $\varepsilon(\omega)$ satisfies the required sum rule (4.32). By contrast, the density of states of the locally propagating modes is less sensitive to the value of m, as a selection of the Bloch waves at symmetry points have their frequencies anchored to m-independent values.

Our analytical results may be compared with numerical calculations [3,15] carried out for the same lattice as illustrated in Fig. 7, but with sheets of nonzero thickness ($d = 0.16a$) and finite relative permittivity ($\varepsilon = 8.9$), leading to the parameter value $m/2a = 0.71$. The published dispersion relations extend up to a frequency given by $\omega a/c \approx 3.8$. In this work, the material relative permittivity had a uniform value, including regions common to two sheets, in contrast to the additive property (4.1) assumed in our analytical model. The calculated band structures resemble those of our Fig. 10, and the resemblance is closer when we take the same value of $m/2a$. The lowest evanescent-wave bands for s polarization in Fig. 1(b) of [3,15] are further distorted from the tight-binding forms, with a small lifting of the degeneracies at Γ and in the Σ direction, but the part of the next higher band visible in this figure is closely similar to the form shown in our Fig. 10(a). There are no absolute band gaps, and the existence of a gap for p polarization alone, with none for s polarization, is explained in terms of the different distributions of fields in dielectric and air at the symmetry point X for the lowest bands in the two polarizations.

The calculations reported here are restricted to propagation in the two-dimensional plane of the lattice, with wave vectors perpendicular to the dielectric sheets and well-defined s and p polarizations. Future work should extend the calculations to propagation at arbitrary angles to the sheets, to obtain the full three-dimensional band structure; such an extension is complicated by the removal of the simple separation of the fields into s and p polarizations when the wave vector has an out-of-plane component. The results would determine the complete density of states of the lattice, and it would be possible to calculate the variation of the atomic spontaneous emission rate as a function of the atomic position and transition frequency. More generally, the analytical methods can be applied to other geometries, for example, triangular and hexagonal lattices, and to three dimensionally periodic structures. However, the vector nature of the electromagnetic fields greatly complicates any more general calculations, particularly in comparison with the corresponding band theories for the scalar electron wave functions, and further extensions of the analytical approach will be limited by these practical difficulties.

ACKNOWLEDGMENTS

We are most grateful to Professor Sir Roger Elliott for advice on the general properties of densities-of-states functions. This research was supported by the United Kingdom Ministry of Defence Corporate Research Program.

[1] J. Opt. Soc. Am. B **10** (1993), special issue on development and applications of materials exhibiting photonic band gaps, edited by C. M. Bowden, J. P. Dowling, and H. O. Everitt.
[2] J. Mod. Opt. **41** (1994), special issue on photonic band structures, edited by G. Kurizki and J. W. Haus.
[3] J. D. Joannopoulos, R. D. Meade, and J. N. Winn, *Photonic Crystals* (Princeton University Press, Princeton, 1995).
[4] *Photonic Band Gap Materials*, edited by C. M. Soukoulis (Kluwer, Dordrecht, 1996).
[5] E. Yablonovitch, T. J. Gmitter, and K. M. Leung, Phys. Rev. Lett. **67**, 2295 (1991); E. Yablonovitch, T. J. Gmitter, R. D. Meade, A. M. Rappe, K. D. Brommer, and J. D. Joannopoulos, *ibid.* **67**, 3380 (1991).
[6] P. Yeh, *Optical Waves in Layered Media* (Wiley Interscience, New York, 1988).
[7] K. M. Leung and Y. F. Liu, Phys. Rev. Lett. **65**, 2646 (1991).
[8] Z. Zhang and S. Satpathy, Phys. Rev. Lett. **65**, 2650 (1991).
[9] M. Ho, C. T. Chan, and C. M. Soukoulis, Phys. Rev. Lett. **65**, 3152 (1991).
[10] J. B. Pendry and A. MacKinnon, Phys. Rev. Lett. **69**, 2772 (1992).
[11] J. B. Pendry, J. Mod. Opt. **41**, 209 (1994).
[12] N. Stefanou, V. Karathanos, and A. Modinos, J. Phys. Condens. Matter **4**, 7389 (1992).
[13] R. K. Angus, D.Phil. thesis, University of Oxford, 1959 (unpublished).
[14] R. de L. Kronig and W. G. Penney, Proc. R. Soc. London Ser. A **130**, 499 (1931).
[15] R. D. Meade, A. M. Rappe, K. D. Brommer, and J. D. Joannopolous, J. Opt. Soc. Am. B **10**, 328 (1993).
[16] T. J. Shepherd and P. J. Roberts, Phys. Rev. E **51**, 5158 (1995).
[17] R. Lang, M. O. Scully, and W. E. Lamb, Phys. Rev. A **7**, 1788 (1973); B. Baseia and H. M. Nussenzweig, Opt. Acta **31**, 39

(1984); J. C. Penaforte and B. Baseia, Phys. Rev. A **30**, 1401 (1984); Phys. Lett. **107A**, 250 (1985); M. Ley and R. Loudon, J. Mod. Opt. **34**, 227 (1987).

[18] M. Born and E. Wolf, *Principles of Optics*, 6th ed. (Pergamon, Oxford, 1993).

[19] P. St. J. Russell, T. A. Birks, and F. D. Lloyd-Lucas, in *Confined Electrons and Photons: New Physics and Applications*, edited by E. Burstein and C. Weisbuch (Plenum, New York, 1994).

[20] J. P. Dowling and C. M. Bowden, Phys. Rev. A **46**, 612 (1992); J. Opt. Soc. Am. B **10**, 353 (1993).

[21] N. W. Ashcroft and N. D. Mermin, *Solid State Physics* (Saunders College, Philadelphia, 1976), Chap. 10.

[22] H. Jones, *The Theory of Brillouin Zones and Electronic States in Crystals* (North-Holland, Amsterdam, 1962), p. 103.

[23] J. P. Dowling and C. M. Bowden, J. Mod. Opt. **41**, 345 (1994).

[24] I. S. Gradsteyn and I. M. Ryzhik, *Tables of Integrals, Series and Products* (Academic, New York, 1980), Sec. 3.62.

[25] M. Altarelli, D. L. Dexter, H. M. Nussenzveig, and D. Y. Smith, Phys. Rev. B **6**, 4502 (1972).